nature electronics

ARTICLES

https://doi.org/10.1038/s41928-017-0001-0

Monitoring vital signs over multiplexed radio by near-field coherent sensing

Xiaonan Hui* and Edwin C. Kan

Monitoring the heart rate, blood pressure, respiration rate and breath effort of a patient is critical to managing their care, but current approaches are limited in terms of sensing capabilities and sampling rates. The measurement process can also be uncomfortable due to the need for direct skin contact, which can disrupt the circadian rhythm and restrict the motion of the patient. Here we show that the external and internal mechanical motion of a person can be directly modulated onto multiplexed radiofrequency signals integrated with unique digital identification using near-field coherent sensing. The approach, which does not require direct skin contact, offers two possible implementations: passive and active radiofrequency identification tags. To minimize deployment and maintenance cost, passive tags can be integrated into garments at the chest and wrist areas, where the two multiplexed far-field backscattering waveforms are collected at the reader to retrieve the heart rate, blood pressure, respiration rate and breath effort. To maximize reading range and immunity to multipath interference caused by indoor occupant motion, active tags could be placed in the front pocket and in the wrist cuff to measure the antenna reflection due to near-field coherent sensing and then the vital signals sampled and transmitted entirely in digital format. Our system is capable of monitoring multiple people simultaneously and could lead to the cost-effective automation of vital sign monitoring in care facilities.

Current approaches to monitoring vital signs are based on body electrodes[1,2], optical absorption[3,4], pressure or strain gauges[5,6], stethoscopes[7,8] and ultrasound[9] or radiofrequency (RF)[10–13] backscattering, each of which suffers particular drawbacks during application. Methods based on body electrodes, such as electrocardiograms, require direct skin contact, and for some people, chest hair may need to be removed to improve the signal quality. For animal tests in rats, pigs and monkeys, hair removal or needle electrodes is almost always required, which complicates the preparation steps and adds to animal discomfort[14,15]. Commercial optical absorption methods, such as photoplethysmography, rely on the reflection or transmission of infrared light, which limits sensing depth and leads to loss of waveform detail and timing accuracy[16]. Strain gauges are usually used for monitoring respiration and blood pressure, but the discomfort of the belt or cuff can be disruptive to the circadian rhythm. Stethoscopes are affected by acoustic wave distortion through tissue and the frequency response of the acoustic transducer. Ultrasound devices are portable but bulky. In acoustic impedance matching the rubbery coating on the probe and water-based gel on the body also cause discomfort when undergoing long-term monitoring. With RF methods, due to the strong reflection of the body's surface and the geometric average of the reflected signal, conventional RF-based far-field vital sign detection can pick up breath motion. However, it is difficult to distinguish small mechanical vibration details such as the heartbeat and wrist-pulse waveforms with low-frequency RF signals[17,18]. Although the heart rate can be retrieved after careful filtering, estimation of blood pressure and the simultaneous monitoring of multiple free-moving people remains unachievable.

We have developed a concept termed near-field coherent sensing (NCS), a method to directly modulate the mechanical motion on the surface and inside a body onto multiplexed radio signals integrated with a unique digital identification (ID). In NCS, more electromagnetic energy is directed into the body tissue than with typical RF methods (where the RF energy is mostly reflected by the body surface), so the backscattered signal from internal organs is implicitly amplified. At the same time, the shorter wavelength inside the body renders a small mechanical motion into a relatively large phase variation, which also increases the sensitivity. NCS can be evaluated at the far-field radiation or at the antenna reflection, offering increased design freedom for the development of different application scenarios in the future.

Principle and implementation of NCS

We use CST Microwave Studio[19] to illustrate our NCS principle. Electromagnetic simulations of a male torso (Fig. 1a) and a lower left arm (Fig. 1b) were constructed[20] (see Methods and Supplementary Fig. 1a for details). The antennas were deployed close to the heart and the left wrist where the pulse can be felt. The signal source should be within the near-field zone of the antennas, but no direct skin contact is required. The antenna is designed to couple more electromagnetic energy into the tissue for a larger signal-to-noise ratio (SNR). To simulate the mechanical motion coupled onto the electromagnetic field, a small vibration was introduced into the geometric scale of the heart and the wrist vessel. The far-field NCS signals were recorded at sampling points 1 m in front of the chest and above the wrist (Supplementary Fig. 2), and the demodulated heart signal and wrist pulse signal were found to match well with the known vibration (Fig. 1c). Transient responses of the co-polarization electric field caused by the heartbeat and the wrist pulse are shown in Supplementary Video 1.

The NCS method uses both the amplitude and phase of the electromagnetic field. Because the phase is very sensitive to the distance between the RF source and receiver, the external chest movement when a person breathes can be evaluated accordingly by the phase. The respiration rate can be easily retrieved and the respiration effort can be further interpreted with the phase variation. In comparison with the phase information, the amplitude of the electromagnetic

School of Electrical and Computer Engineering, Cornell University, Ithaca, NY, USA. *e-mail: xh273@cornell.edu

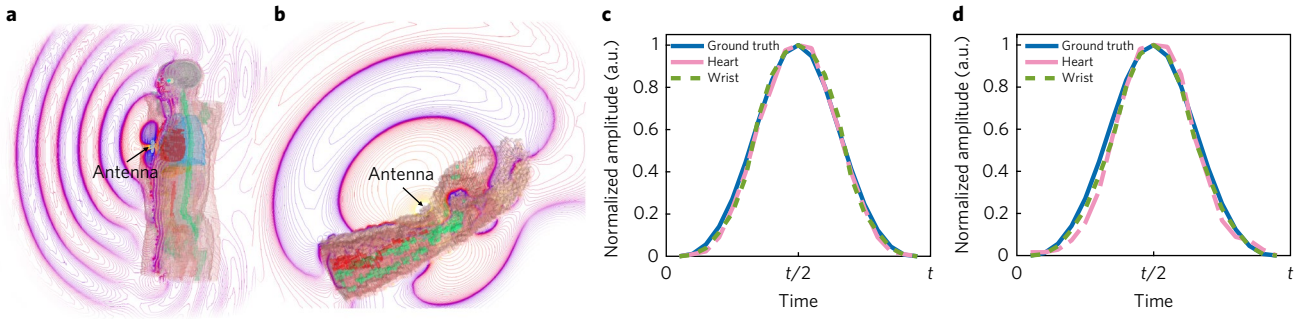

Fig. 1 | CST Microwave Studio simulation model for monitoring vital signs over radio transmission by near-field coherent sensing. a,**b**, Electromagnetic simulations of a male torso (**a**) and a lower left arm (**b**). The patterns shown are the real part of the co-polarization electric field in the torso simulation model for heartbeat sensing (**a**) and in the wrist simulation model for pulse sensing (**b**). Animated simulations of these conditions are shown in Supplementary Video 1. **c**,**d**, Simulated beating amplitudes of the heart and wrist, compared with sampling at the far-field points (**c**) and at the antenna reflection represented by the scattering parameter S_{11} (**d**). Normalized beating amplitudes are shown as blue solid lines. Demodulated heart signals are shown as pink dashed lines and wrist pulse signals as green dotted lines. Far-field signals were recorded at the sampling points 1 m in front of the chest and above the wrist, as shown in Supplementary Fig. 2.

field is not so sensitive to the small distance variation, which means the breath or other external body movement will change the phase but not the amplitude as much, providing good isolation for other signals inside the body to be properly sensed. In NCS, the interferometry-like structure transduces the internal organs/tissues movement into amplitude modulation of the RF signal.

For our simulations (Fig. 1a), when the human phantom faces the receiver (Supplementary Fig. 2a), the on-chest antenna emits the RF carrier with the antenna characteristics defined by the local near-field region. According to the antenna directivity, part of the RF energy will be directly emitted towards the receiver, while the other part will be coupled inside the body due to the near-field effect. Intuitively, we can consider that the backscattered RF signal from the heart is modulated by the mechanical movement of the heart tissue and then interferes with the direct emission, resulting in amplitude changes. From the interferometer analogy, the movement inside the body is a 'differential-mode' modulation, while the body surface movement is a 'common-mode' modulation. The two signals can be easily distinguished (for further explanation see Supplementary Fig. 1a).

In addition to the far-field implementation, the motion can also be derived from the antenna reflection, which is shown as the scattering parameter S_{11} in Fig. 1d. The NCS signal measured by antenna reflection can be directly recorded on the mobile unit and is therefore more immune to body movement and indoor multipaths in a crowded room. Because the tissue motion is within the near-field region of the antenna, the geometric variation will affect the antenna reflection S_{11}, where the antenna can be regarded as a part of the sensor. The vital signs will be modulated on the antenna's S_{11} parameter and retrieved by the reflected signal accordingly.

An essential part of our NCS method and its ability to modulate vital signals over radio is a transmitting antenna close to the skin. However, a conventional microwave transmitter consumes significant power in the local oscillator and power amplifier, so a battery is required for a mobile device. In addition, synchronization between the on-body transmitter and the far-field receiver will also make the system design more complex. We chose to implement NCS by passive harmonic RF identification (RFID) tags[21], where the vital signals are modulated on the harmonic backscattering together with the tag ID. Besides the ultralow cost, the simple and robust packaging of the passive tag enables direct fabric integration with laundry readiness[22,23]. An example of the RFID sensor tag chip integrated with an embroidered antenna on fabric is shown in Supplementary Fig. 4a. The benefits of harmonic backscattering over the conventional RFID are summarized in Supplementary Fig. 3. Because of the high transmitting power of the conventional RFID reader and the phase noise skirt, the self-leakage, antenna reflection and the backscattering from unintended ambient objects all contribute to the noise and heavily degrade the SNR of the backscattered tag signal. However, the harmonic backscattering can isolate the

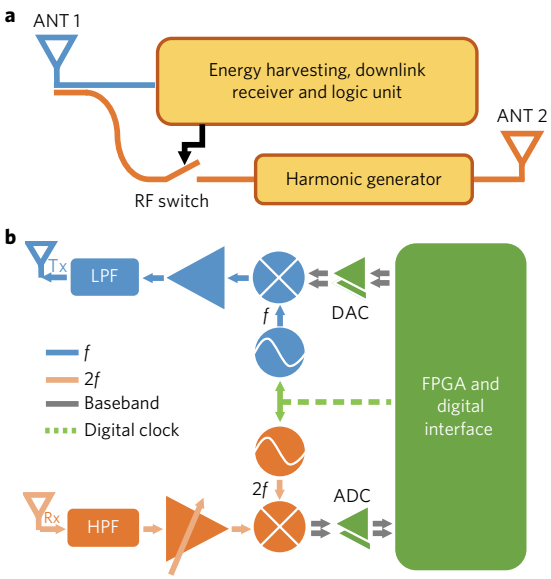

Fig. 2 | Schematics of harmonic RFID system for near-field coherent sensing. a, Passive harmonic RFID tag. The harmonic tag receives the downlink RF signal (at frequency *f*) from the reader. It goes through the tag Antenna 1 (ANT 1) and splits into two parts: one provides d.c. power for tag circuits by energy harvesting and the other is fed into the passive harmonic generator (at frequency 2*f*) to be re-emitted from Antenna 2 (ANT 2). **b**, Schematic of the harmonic RFID reader. The digital clock is fed into two frequency synthesizers at *f* and 2*f* for coherent demodulation at 2*f*. The digital module performs the code-division multiple-access (CDMA) protocol[25]. The downlink commands from the reader to tags are modulated by the digital-to-analogue converter (DAC) and then upconverted by the mixer (blue) to the carrier at *f*. The harmonic tag backscatters to the reader at 2*f*, which is downconverted to the base band by the coherent local oscillator at 2*f* and sampled by the quadrature analogue-to-digital converter (ADC). Tx, transmitter; Rx, receiver; LPF, low-pass filter; HPF, high-pass filter; FPGA, field programmable gate array.

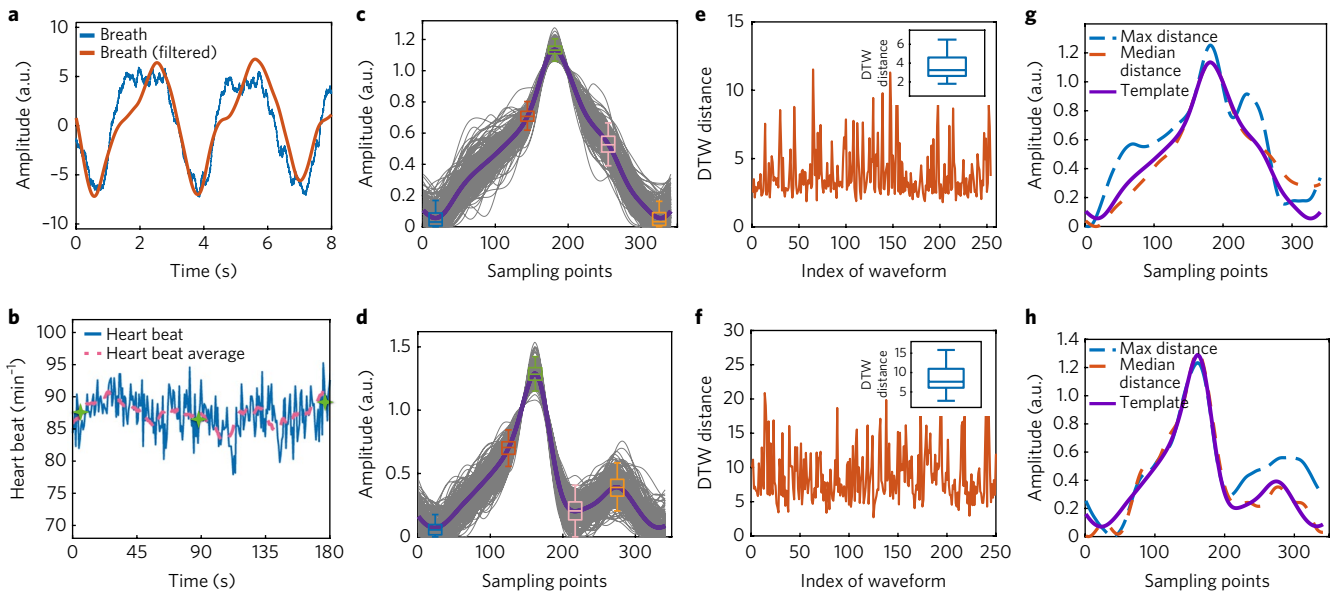

Fig. 3 | The vital signals from NCS measurements. a, Raw breath signal and waveform after the low-pass filter. **b**, Raw heart rates and the average from the moving window of 10 s. Green markers show measurements from the OMRON blood pressure monitor mounted on the left forearm. **c**,**d**, Waveforms of heartbeat (**c**) and wrist pulse (**d**) during data collection for 3 min. The purple lines are the average waveforms of the 3-min data. The box-whisker plots in **c** are the statistical results at the minimum point (blue), rising deflection point (red), maximum point (green), falling deflection point (pink) and local minimum point (yellow). The box-whisker plots in **d** are at the minimum point (blue), rising deflection point (red), maximum point (green), local minimum point (pink), and local maximum point (yellow). **e**,**f**, DTW waveform analyses show the distance in each waveform of the heartbeat (**e**) and the wrist pulse (**f**). Insets: box-whisker distributions. **g**,**h**, Comparison of median- and maximum-distance waveforms with respective DTW template for the heartbeat (**g**) and wrist pulse (**h**). Sampling rate for the waveforms: 500 Sps.

downlink (reader-to-tag) and uplink (tag-to-reader) with a large frequency separation, which increases both the SNR and sensitivity. The tag remains a passive backscatterer, which can easily comply with current RF protocols. A schematic of the harmonic tag[24] is shown in Fig. 2a (for a photograph of the printed circuit board (PCB) prototype see Supplementary Fig. 4b). The harmonic tag receives the downlink RF signal at f from the reader, which goes through the tag Antenna 1 (ANT 1) and splits into two parts. One provides d.c. power for the tag circuits by energy harvesting, and the other is fed into passive harmonic generation at $2f$ to be re-emitted from Antenna 2 (ANT 2), which serves as the NCS transmitter. The RF switch in front of the harmonic generator can modulate digital information by on–off keying (OOK), similar to conventional RFID operations. The digital information can include the tag ID as well as additional information from the on-tag sensors.

The schematic of the harmonic RFID reader as a coherent transceiver is shown in Fig. 2b. The same digital clock (green dash line) is fed into two frequency synthesizers at f and $2f$ for coherent demodulation at $2f$. The digital module performs the code-division multiple-access (CDMA) protocol[25]. The downlink commands from the reader to tags are modulated by the digital-to-analogue converter (DAC), and then upconverted by the mixer (blue) to the carrier at f. The harmonic tag backscatters to the reader at $2f$, which is downconverted to the base band by the coherent local oscillator at $2f$ and sampled by the quadrature analogue-to-digital converter (ADC). The hardware of the harmonic reader is conducted with the software defined radio (SDR).

Analyses of the NCS signal

The phase modulation is very sensitive to the physical location of the tag with respect to the reader. Hence, when Antenna 2 of the tag is placed on the chest, the breath information can be derived from the phase in the quadrature scheme, as shown in Fig. 3a with raw and low-pass-filtered waveforms. Based on the backscattered phase information, the positions of multiple tags can be calculated with millimetre resolution[25,26] (Supplementary Fig. 5), which can further derive the respiratory effort. Although the phase variation caused by the chest movement is much stronger than the internal movement of the heartbeat and wrist pulse, it is a 'common component' for NCS. During our experiments, the NCS heartbeat signal was modulated on amplitude and is thus immune to the breath movement. Multiple frequencies, improved signal processing and reflection structure (Supplementary Fig. 6) can further help mitigate heavy multipath interference. As shown in Fig. 3b, we first retrieved the heart rate from the instantaneous period (blue solid line) and from the counts within 10 s (pink dashed line). The green markers were measured with a commercial blood pressure monitor (OMRON BP760N). Note that the breath and heartbeat information is independently derived from the quadrature demodulation, and no special filtering or pattern recognition as in the conventional microwave backscattering is required[27,28].

Because the internal vital signals are retrieved from NCS, the interferometer-like structure significantly increases the sensitivity to enable collection of the motion waveform, similar to a ballistocardiogram (BCG)[29]. We recorded data from the chest and wrist tags simultaneously for 3 min. The experiments were conducted with the PCB tag and the reader antenna was ~1.5–2 m away from the person under test. The harmonic signal converted by the tag was about −20 dBm at 1.9 GHz ($2f$). To analyse the waveform variation, each period was overlaid to obtain the average and box-whisker deviation of the heartbeat and wrist-pulse waveforms (Fig. 3c,d). The waveforms are normalized to the 90th percentiles of the recorded data and the box-whisker plots show the variations of the feature points. We further applied the dynamic time warping (DTW) to sort the waveforms to derive the detailed features[30]. Figure 3e,f shows the DTW distance for the heart and pulse waveforms and the insets show the variations. Figure 3g,h, presents a comparison of the extracted template waveforms with the maximum-distance

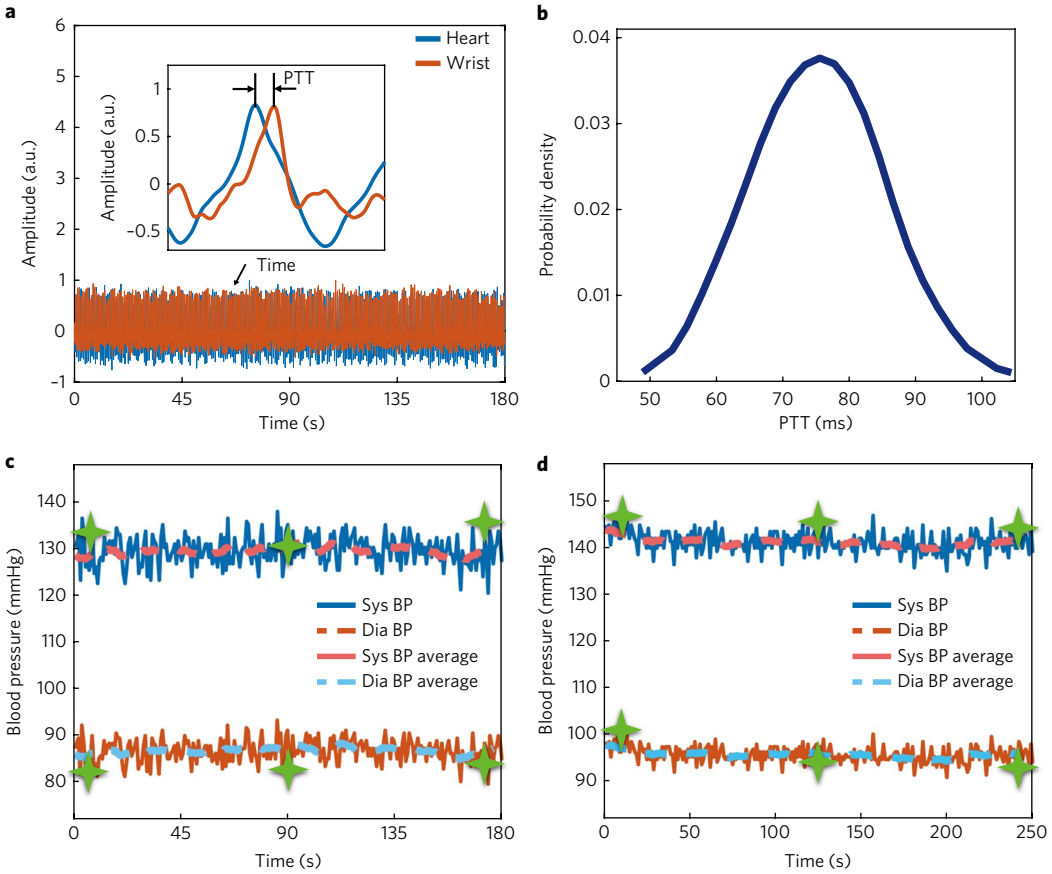

Fig. 4 | Blood pressure measured by NCS. a, Pulse transit time (PTT) estimated from the synchronized heartbeat (blue) and wrist pulse (red) waveforms. Inset: one period of the signals and the extracted PTT. **b**, Probability density distribution of the PTT over 3 min. **c**,**d**, Blood pressure extracted from the PTT when the person under test is seated (**c**) and when the person under test goes through moderate activity and is standing (**d**). Green markers show blood pressures measured using a commercial blood pressure monitor. Blue and red solid lines are systolic (Sys) and diastolic (Dia) pressures (BP) of every heartbeat. Pink and light blue dashed lines are moving averages from 14 sampling points around 10 s.

and median-distance waveforms; the latter still closely resemble the template and keep most of the major features, such as the recoil peak in the wrist pulse. The detailed motion waveform analysis can be a cardiogram candidate for arrhythmia and aortic valvular diseases[31]. A real-time waveform recording is shown in Supplementary Fig. 7 and Supplementary Video 2.

The CDMA protocol enables simultaneous monitoring of multiple persons and also multiple points on the same person. The allowable number of CDMA tags is limited by the baseband data rate and is shown in Supplementary Fig. 8. Comparison of the waveform timing from different body positions offers estimates of the blood pressure (BP) through the pulse transit time (PTT), which can be extracted from the feature points of the proximal and distal arterial waveforms[32,33]. Our non-contact sensing of blood pressure presents significant advantages over direct pressure-based methods, which cause discomfort and disrupt the circadian rhythm, especially in long-term monitoring of elderly patients. We recorded the chest tag signal as the proximal waveform and the left wrist tag signal as the distal waveform for 3 min, as shown in Fig. 4a. PTT can be readily extracted from the major peaks of the two waveforms. Figure 4b shows the probability density of the PTT during the 3 min recording. The distribution of the PTT may be affected by sampling jitter and waveform distortion. We can obtain one PTT sample for each heartbeat, and the moving average or other signal-processing methods can be readily applied to minimize the PTT variation. Figure 4c,d shows the blood pressures calculated from the PTT as well as comparison points from the commercial blood pressure monitor (OMRON BP760N). The data in Fig. 4c were collected when the person under test sat on a chair for about 30 min, while the data in Fig. 4d were collected after moderate activity.

Conclusions

We have developed a method for monitoring vital signs that modulates the detailed motion on and inside the body onto multiplexed RF signals through NCS. The shorter wavelength inside the body naturally increases the SNR of the sensed mechanical motion. In addition, the differential nature of the internal movement isolates the large surface movement, which also increases the sensitivity to enable the collection of weak motion from the wrist pulse. NCS can be implemented as passive tag backscattering or as active tag antenna reflection. The ready multiplexing technique in passive and active RF transmission facilitates simultaneous sensing for multiple points and multiple persons. NCS opens up new opportunities for vital sign monitoring with accuracy, comfort, convenience and low cost.

Methods

We used CST Microwave Studio[19] for electromagnetic simulation. Zubal Phantom[20] was used to construct the dielectric models. The tissue geometric information was calibrated with data from computed tomography (CT) and magnetic resonance imaging (MRI). The resolution of the voxel was 3.6 mm × 3.6 mm × 3.6 mm. The microwave properties of various tissues were mapped with CST Bio-library. We first pre-processed the Zubal Phantom data into the file structure of tissue geometric coordinates together with the tissue indices, layer by layer. CST then imported the files and automatically built every voxel with the three-dimensional coordinates and tissue properties to establish the dielectric model controlled by

the scripts of CST built-in Visual Basic for Applications (VBA) Macro language. The process is analogous to three-dimensional printing, but only virtually in the CST software. Dynamic simulations of heartbeats and wrist pulses were realized by geometrical variations, where the geometries of the heart and the wrist vessel were changed according to the preset dimension serving as the ground truth.

The passive harmonic backscattering tag was prototyped by a custom PCB[24] as shown in the Supplementary Information, modified from the Wireless Identification and Sensing Platform (WISP)[34]. The harmonic generator on the tag was designed with a nonlinear transmission line (NLTL)[21], which consists of a ladder structure of inductors and varactors. The NLTL can provide high conversion efficiency with low input power, which is essential for passive backscattering tag design. The harmonic RFID reader and the antenna reflection system were built on the platform of National Instrument Ettus Software Defined Radio (SDR) B210. To realize coherent harmonic demodulation, the local oscillator (LO) of the receiver needed to be directly derived from the second harmonic frequency of the transmitter LO. The real-time control and demodulation software was composed in LabVIEW. The operating frequency was $f = 950$ MHz (second harmonic at $2f = 1.9$ GHz) with the homodyne modulation scheme. The downlink analogue baseband was 10 kHz and the uplink analogue baseband after harmonic conversion was 20 kHz. Both digital-to-analogue and analogue-to-digital conversions operate at 10^6 samples per second (Sps). The raw digital signals were then filtered, digitally downconverted to the d.c. band, and decoded with the CDMA algorithm to distinguish the information from each tag. The signal from each tag was then downsampled by the sampling rate of 500 Sps. The breath signal was processed by a low-pass filter with a cutoff frequency of 0.8 Hz. The heartbeat and pulse signals were processed by the bandpass filter between 0.9 Hz and 15 Hz. The present operating range for the passive tag is ~1.5 m, limited by the WISP platform. The range can be extended towards 10 m according to the operation of conventional RFID systems in the same frequency band.

Data availability. The data that support the plots within this paper and other findings of this study are available from the corresponding author upon reasonable request.

Received: 22 May 2017; Accepted: 16 October 2017;
Published online: 27 November 2017

References

1. Patterson, R. P. Fundamentals of impedance cardiography. *IEEE Eng. Med. Biol. Mag.* **8**, 35–38 (1989).
2. Payne, R. A., Symeonides, C. N., Webb, D. J. & Maxwell, S. R. J. Pulse transit time measured from the ECG: an unreliable marker of beat-to-beat blood pressure. *J. Appl. Physiol.* **100**, 136–141 (2006).
3. Allen, J. Photoplethysmography and its application in clinical physiological measurement. *Physiol. Meas.* **28**, R1 (2007).
4. Tamura, T., Maeda, Y., Sekine, M. & Yoshida, M. Wearable photoplethysmographic sensors—past and present. *Electronics* **3**, 282–302 (2014).
5. Gong, S. et al. A wearable and highly sensitive pressure sensor with ultrathin gold nanowires. *Nat. Commun.* **5**, 3132 (2014).
6. Pang, C. et al. A flexible and highly sensitive strain-gauge sensor using reversible interlocking of nanofibres. *Nat. Mater.* **11**, 795–801 (2012).
7. Kindig, J. R., Beeson, T. P., Campbell, R. W., Andries, F. & Tavel, M. E. Acoustical performance of the stethoscope: a comparative analysis. *Am. Heart J.* **104**, 269–275 (1982).
8. Liang, H., Lukkarinen, S. & Hartimo, I. Heart sound segmentation algorithm based on heart sound envelogram. *Comput. Cardiol.* http://doi.org/b2q9xp (1997).
9. Frinking, P. J., Bouakaz, A., Kirkhorn, J., Cate, F. J. T. & Jong, N. Ultrasound contrast imaging: current and new potential methods. *Ultrasound Med. Biol.* **26**, 965–975 (2000).
10. Lin, J. C. Noninvasive microwave measurement of respiration. *Proc. IEEE* **63**, 1530 (1975).
11. Chen, K., Misra, D., Wang, H., Chuang, H. & Postow, E. An X-band microwave life-detection system. *IEEE Trans. Biomed. Eng.* **7**, 697–701 (1986).
12. Li, C. et al. A review on recent progress of portable short-range noncontact microwave radar systems. *IEEE Trans. Microw. Theory Tech.* **65**, 1692–1706 (2017).
13. Celik, N., Gagarin, R., Huang, G. C., Iskander, M. F. & Berg, B. W. Microwave stethoscope: development and benchmarking of a vital signs sensor using computer-controlled phantoms and human studies. *IEEE Trans. Biomed. Eng.* **61**, 2341–2349 (2014).
14. Wolf, R. H., Lehner, N. D. M., Miller, E. C. & Clarkson, T. B. Electrocardiogram of the squirrel monkey *Saimiri sciureus*. *J. Appl. Physiol.* **26**, 346–351 (1969).
15. Pereira-Junior, P. P., Marocolo, M., Rodrigues, F. P., Medei, E. & Nascimento, J. H. M. Noninvasive method for electrocardiogram recording in conscious rats: feasibility for heart rate variability analysis. *An. Acad. Bras. Cienc.* **82**, 431–437 (2010).
16. Kamal, A. A. R., Harness, J. B., Irving, G. & Mearns, A. J. Skin photoplethysmography—a review. *Comput. Methods Programs Biomed.* **28**, 257–269 (1989).
17. Chen, K., Huang, Y., Zhang, J. & Norman, A. Microwave life-detection systems for searching human subjects under earthquake rubble or behind barrier. *IEEE Trans. Biomed. Eng.* **47**, 105–114 (2000).
18. Kao, T. J., Yan, Y., Shen, T., Chen, A. Y. & Lin, J. Design and analysis of a 60-GHz CMOS Doppler micro-radar system-in-package for vital-sign and vibration detection. *IEEE Trans. Microw. Theory Tech.* **61**, 1649–1659 (2013).
19. CST Microwave Studio (Computer Simulation Technology, 2017); http://www.cst.com
20. Zubal, I. G. et al. Computerized three-dimensional segmented human anatomy. *Med. Phys.* **21**, 299–302 (1994).
21. Yu, F., Lyon, K. G. & Kan, E. C. A novel passive RFID transponder using harmonic generation of nonlinear transmission lines. *IEEE Trans. Microw. Theory Techn.* **58**, 4121–4127 (2010).
22. Patron, D. et al. On the use of knitted antennas and inductively coupled RFID tags for wearable applications. *IEEE Trans. Biomed. Circuits Syst.* **10**, 1047–1057 (2016).
23. Gordon, P. H., Chen, R., Park, H. & Kan, E. C. Embroidered antenna characterization for passive UHF RFID tags. Preprint available at https://arxiv.org/abs/1710.02237 (2017).
24. Ma, Y., Hui, X. & Kan, E. C. Harmonic-WISP: a passive broadband harmonic RFID platform. *Proc. Microw. Symp. (IMS), 2016 IEEE MTT-S Int.* 1–4 (IEEE, 2016).
25. Hui, X., Ma, Y. & Kan, E. C. Real-time code-division multi-tag localization with centimeter accuracy. *Proc. IEEE RFID Conf.* 110–116 (IEEE, 2017).
26. Ma, Y., Hui, X. & Kan, E. C. 3D real-time indoor localization via broadband nonlinear backscatter in passive devices with centimeter precision. *Proc. 22nd Int. Conf. Mobile Comput. Network.* 216–229 (ACM, 2016).
27. Li, C., Lubecke, V. M., Boric-Lubecke, O. & Lin, J. A review on recent advances in Doppler radar sensors for noncontact healthcare monitoring. *IEEE Trans. Microw. Theory Techn.* **61**, 2046–2060 (2013).
28. Adib, F., Mao, H., Kabelac, Z., Katabi, D. & Miller, R. C. Smart homes that monitor breathing and heart rate. *Proc. 33rd ACM Conf. Hum. Fact. Comput. Syst.*837–846 (ACM, 2015).
29. Pinheiro, E., Postolache, O. & Girão, P. Theory and developments in an unobtrusive cardiovascular system representation: ballistocardiography. *Open Biomed. Eng. J.* **4**, 201–216 (2010).
30. Sakoe, H. & Chiba, S. Dynamic programming algorithm optimization for spoken word recognition. *IEEE Trans. Acoust. Speech Signal Process* **26**, 43–49 (1978).
31. Kim, C. et al. Ballistocardiogram: mechanism and potential for unobtrusive cardiovascular health monitoring. *Sci. Rep.* **6**, 31297 (2016).
32. Geddes, L. A., Voelz, M. H., Babbs, C. F., Bourland, J. D. & Tacker, W. A. Pulse transit time as an indicator of arterial blood pressure. *Psychophysiology* **18**, 71–74 (1981).
33. Mukkamala, R. et al. Toward ubiquitous blood pressure monitoring via pulse transit time: theory and practice. *IEEE Trans. Biomed. Eng.* **62**, 1879–1901 (2015).
34. Yeager, D. J., Sample, A. P. & Smith, J. R. in *RFID Handbook: Applications, Technology, Security, and Privacy* (eds Ahson, S. & Ilyas, M.) 261–278 (CRC Press, Boca Raton, 2008).

Acknowledgements

This project was supported by the US Department of Energy (DoE) under Advanced Research Projects Agency – Energy (ARPA-E) project no. DE-AR0000528. The authors thank F. Rana and J. Fan for their comments on critical applications and technical presentation, as well as H. Park for assistance with the embroidered antenna.

Author contributions

X.H. formulated the NCS theory, performed the electromagnetic simulation and designed the experimental procedure for conceptual demonstration and calibration. E.C.K. envisioned the NCS principle, set the project goals and coordinated other project activities.

Competing interests

The authors declare no competing financial interests.

Additional information

Supplementary information is available for this paper at https://doi.org/10.1038/s41928-017-0001-0.

Reprints and permissions information is available at www.nature.com/reprints.

Correspondence and requests for materials should be addressed to X.H.

Publisher's note: Springer Nature remains neutral with regard to jurisdictional claims in published maps and institutional affiliations.